Materials Advances

PAPER

View Article Online
View Journal | View Issue

Check for updates

Cite this: *Mater. Adv.*, 2025, **6**, 5171

Enhanced adsorption of Orange G dye using activated diatomite: a novel functionalization approach

Youssef Ettahiri, *[ab] Ayoub Aziz,[c] Khadija Felaous,[c] Abdessalam Bouddouch,[d]
Brahim Akhsassi,[a] Lahcen Bouna,[a] Abdeljalil Benlhachemi[a] and
Luis Pérez-Villarejo [be]

Received 24th May 2025,
Accepted 20th June 2025

DOI: 10.1039/d5ma00536a

rsc.li/materials-advances

This research explores the effectiveness of cetyltrimethylammonium bromide (CTAB)-modified diatomite-based alkali-activated material (GP-DR@CTAB) for removing the organic contaminant Orange G (OG) from polluted water through adsorption. The samples were extensively characterized using techniques including X-ray diffraction (XRD), X-ray photoelectron spectroscopy (XPS), Fourier-transform infrared spectroscopy (FTIR), thermogravimetric analysis/differential thermal analysis (TGA/DTA), Brunauer–Emmett–Teller (BET), scanning electron microscopy (SEM), and transmission electron microscopy (TEM). XRD confirmed the activation of diatomite, while XPS and FTIR verified the successful incorporation of CTAB into the alkali-activated matrix. The GP-DR@CTAB exhibited a significantly higher surface area (107.13 m^2 g^{-1}) compared to the unmodified material (15.92 m^2 g^{-1}). The pseudo second order kinetic model best described the adsorption kinetics for both DR and GP-DR@CTAB, as evidenced by the highest correlation coefficients (R^2 = 0.9901 and 0.9993, respectively) and the close agreement between the experimental and calculated adsorption capacities. Both the Langmuir and Freundlich adsorption isotherms were tested, and the Langmuir model showed the highest correlation with the experimental data. Overall, the results confirm that GP-DR@CTAB is a highly effective and promising adsorbent for the removal of OG from water.

1. Introduction

In recent years, environmental pollution caused by the excessive discharge of toxic organic molecules from various industrial sources has emerged as a critical global issue.[1–5] Industries such as pharmaceuticals, textiles, and agriculture release significant quantities of harmful organic compounds into water bodies, severely impacting ecosystems and human health.[6–9] Azo dyes, such as Orange G, are considered toxic due to the release of harmful aromatic amines in the effluent. They are potentially carcinogenic and can cause serious health effects.[10] Traditional treatment methods, including physical, photochemical, and biological processes, have proven inadequate in completely removing these persistent organic pollutants from water.[11–13] Certain conventional approaches often fall short due to limitations in efficiency, high operational costs, and their inability to degrade complex and stable organic molecules.[14,15] Consequently, there is an urgent need to develop more effective and sustainable water treatment technologies to address this growing environmental challenge.[16,17] Among various treatment methods, adsorption stands out as a highly effective process for removing toxic organic pollutants from water. This technique utilizes materials like activation materials to capture and concentrate contaminants, achieving high removal efficiencies even for complex molecules. Its adaptability, cost-effectiveness, and ability to treat diverse pollutants make adsorption a leading solution in addressing the challenges posed by persistent organic pollutants.[18,19] An emerging alternative for addressing organic pollutants in water is the use of alkali-activated, also known as geopolymer.[20,21] These innovative green materials are synthesized through the activation of aluminosilicate sources with alkaline solutions, such as sodium hydroxide or potassium hydroxide. The preparation process involves mixing

---

[a] Materials and Environment Laboratory (LME), Faculty of Sciences, Ibn Zohr University, Dakhla city B.P. 8106, Agadir, Morocco. E-mail: ettahiriyoussefo@gmail.com
[b] Center for Advanced Studies in Earth Sciences, Energy and Environment (CEACTEMA), University of Jaén, Campus Las Lagunillas, s/n, 23071, Jaén, Spain
[c] Geo-Biodiversity and Natural Patrimony Laboratory (GEOBIO), Scientific Institute, "Geophysics, Natural Patrimony and Green Chemistry" Research Center (GEOPAC), Mohammed V University in Rabat, Avenue Ibn Batouta, P.B. 703, 10106, Rabat-Agdal, Morocco
[d] Laboratory of Physical Chemistry of Materials (LPCM), Department of Chemistry, Faculty of Science, Chouaïb Doukkali University, El Jadida, Morocco
[e] Department of Chemical, Environmental, and Materials Engineering, Higher Polytechnic School of Linares, University of Jaen, Campus Científico-Tecnológico, Cinturón Sur s/n, 23700, Linares, Spain

raw materials like fly ash, metakaolin, or slag with the alkaline activators to form a gel-like binder.[22] Upon curing, the gel undergoes polymerization, resulting in a solid, porous material with high surface area and adsorption capacity.[23,24] Alkali-activated materials are lauded for their environmental benefits, including the utilization of industrial by-products and reduced carbon footprint compared to conventional materials. Their unique structure and chemical properties make them effective at capturing a wide range of organic pollutants, offering a sustainable and efficient solution for water treatment challenges.[25]

Porous alkali-activated are advanced materials that can be effectively used for environmental applications, including the adsorption of organic pollutants. To prepare porous alkali-activated, a typical method involves incorporating pore-forming agents, such as organic foaming agents or templating materials, into the alkali-activated mix. Common pore-forming agents include polyethylene microspheres or expanded perlite, which create voids during the curing process. Additionally, chemical agents like sodium bicarbonate or hydrogen peroxide can be used to generate gas bubbles, further increasing porosity. The alkali-activated precursor, often composed of aluminosilicate sources, is mixed with an alkaline activator, and the pore-forming agents. Upon curing, the alkali-activated solidifies into a lightweight, porous structure with enhanced surface area and porosity. Modifying agents such as surfactants (*e.g.*, cetyltrimethylammonium bromide) or functional polymers (*e.g.*, polyvinyl alcohol) can also be added to enhance their adsorption capabilities for organic pollutants.[26] Organic polar compounds, known as surfactants, possess both hydrophilic and hydrophobic groups and are extensively utilized in industrial applications.[27,28] Among them, CTAB is highly regarded as an effective stabilizing agent for the synthesis of advanced nanomaterials.[29,30] CTAB, a surfactant, modifies the surface properties of alkali-activated by increasing their hydrophobicity and surface area. This modification facilitates better interaction and uptake of nonpolar organic contaminants, improving the overall efficiency of the adsorption process.[31] Açışlı *et al.*[32] used the CTAB to modify a fly ash-based geopolymer for the adsorption of the anionic dye Acid Blue 185. Bouna *et al.*,[23] on the other hand, utilized hydrogen peroxide (H_2O_2) as a blowing agent for direct foaming, with CTAB serving to stabilize the gas bubbles formed during geopolymerization.

The primary objective of this study is to investigate diatomite as a geomaterial precursor, rich in amorphous silica and characterized by a microporous structure, for the preparation of alkali-activated diatomite functionalized with cetyltrimethylammonium bromide (CTAB). The study aims to evaluate its potential for removing the organic pollutant Orange G (OG) from contaminated water. Structural characterizations of the adsorbent were conducted to analyze its morphology and surface properties. Additionally, various experimental tests were carried out to investigate the adsorption mechanism at the solid–liquid interface, focusing on *in situ* electrostatic interactions to provide deeper insights into the underlying adsorption processes.

2. Materials and methods

2.1. Materials

Diatomite rock. Diatomite (DR) is often referred to as kieselguhr or diatomaceous earth, is a sedimentary rock rich in silica characterized by its microporous structure. This rock primarily consists of the siliceous frustules of diatoms, which are unicellular microalgae that thrive in aquatic environments, ranging in size from 2 μm to 1 mm. Upon the death of these microalgae, their silica shells settle on the seabed, leading to the accumulation and fossilization of thick layers of diatom shells into diatomaceous earth. In Morocco, there are two known diatomite deposits: one located near the volcanic regions of the eastern Rif and another in central Morocco, both dating from the tertiary to quaternary periods. The diatomite examined in this study originates from a deposit in central Morocco, specifically from the Aouinet deposit in the Oulmès area. This site is notable for its high-quality, pure white diatomite. The extracted diatomite was taken from a layer consisting entirely of this material and was processed into a fine fraction (less than 63 μm) using a ball mill and vibrating sieve.

Activating solution. Alkaline activation of diatomaceous earth was achieved using a combination of sodium hydroxide (NaOH) and sodium silicate (Na_2SiO_3). To prepare an 8 M NaOH solution, 98% of pure NaOH flakes were dissolved in distilled water using a magnetic stirrer. This NaOH solution was then mixed with sodium silicate gel in a Na_2SiO_3/NaOH ratio equal to 1. The resulting mixture was left to stand for 24 hours before being used for diatomite activation.

2.2. Alkali-activated materials preparation

Two types of alkali-activated materials GP-DR and GP-DR@CTAB were synthesized in this study using diatomite powder, a pre-prepared activating solution, and a surfactant known as cetyltrimethylammonium bromide (CTAB) (Fig. 1). Initially, the reference sample (GP-DR) was synthesized by mixing diatomite powder with the activating solution at a liquid-to-solid ratio of 1.2. The mixture was kneaded for 15 minutes, poured into molds, and allowed to cure at room temperature. Subsequently, the CTAB-containing material was synthesized by dissolving 1% (mass percentage) of CTAB in the previously prepared activating solution and stirring for 5 minutes. The prepared solution was then mixed with diatomite powder at the same liquid-to-solid ratio of 1.2, agitated for 15 minutes, poured into molds, and left to cure at room temperature. After 48 hours, both hardened materials were separately ground and washed multiple times with distilled water to remove any unreacted soluble substances. The samples were collected through centrifugation, dried, and ground again to facilitate structural characterization and adsorption testing.

2.3. Characterizations methods

The XRD data for various alkali-activated preparations were obtained by measuring diffraction patterns using a PANalytical Empyrean instrument equipped with a PIXcel-3D detector, and peak identification was performed using HighScore software.

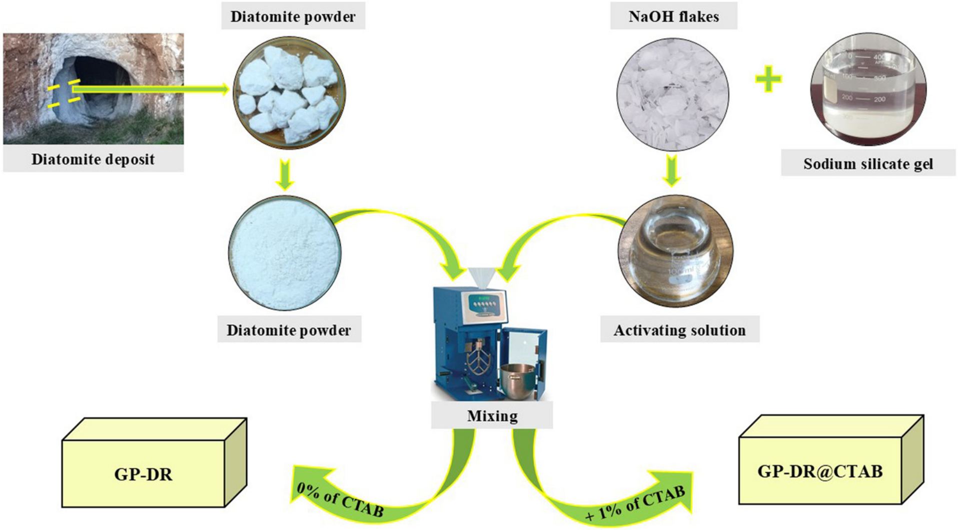

Fig. 1 Schematic illustration of alkali-activated prepared.

FTIR spectra were obtained using a Nicolet iS10 Thermo Scientific instrument. The chemical composition of the surface samples was studied using the XPS Phoibos 150 MCD. To compensate for charge, all spectra were calibrated against aliphatic carbon (C(1 s)) at 285 eV before curve fitting, and the deconvolution of individual XPS peaks was performed using Casa XPS software. For TGA and DTA analyses, a Q500 TA instrument was employed. The DR and GP-DR samples were subjected to temperature ranges of 25 to 1000 °C with a temperature increase of 10 °C per minute. N_2 adsorption/desorption experiment was conducted using liquid nitrogen at −196 °C. This isotherm was utilized to calculate the BET surface area and estimate the total pore volume at a relative pressure of 0.98. The average pore size of the sample was determined using the BJH desorption method. Scanning electron microscopy (SEM) analyses were performed using an FEI Quanta 200-ESEM, operated at 20 kV and Transmission Electron Microscopy (TEM, Philips CM 200).

3. Results and discussion

3.1. Characterization

Fig. 2a presents the X-ray diffraction (XRD) data for the diatomite raw rock (DR) and two different alkali-activated prepared GP-DR and GP-DR@CTAB. In the XRD pattern of the DR sample, prominent reflections from (SiO_2, JCPDS:96-900-9667) and calcite ($CaCO_3$, JCPDS: 05-0586) can be observed. In the synthesized alkali-activated samples GP-DR and GP-DR@CTAB, an amorphous hump is visible in the 15–36° 2θ angular range, indicating successful alkali activation and transformation of the diatomite rock into an alkali-activated gel.[33] Additionally, the XRD pattern displays sharp peaks corresponding to residual crystalline phases originating from the diatomite rock precursor, possibly calcium silicates or calcium aluminates.[34]

The XPS technique was used to study the surface chemistry of DR and GP-DR@CTAB. The XPS survey spectra of these samples are depicted in Fig. 2b. From the Fig, it is evident that the XPS survey of DR exhibits the detection of multiple elements, including oxygen (O 1s, OKLL), silicon (Si 2s, Si 2p), carbon (C 1s), and aluminum (Al 2s, Al 2p).[35–37] Likewise, the XPS survey of GP-DR@CTAB demonstrates the characteristic peaks corresponding to carbon (C 1s), oxygen (O 1s, OKLL), silicon (Si 2s, Si 2p), aluminum (Al 2s, Al 2p), nitrogen (N 1s), and bromine (Br 3d). Notably, the presence of certain groups such as C–NH and ($-N^+(CH_3)_2/-N^+(CH_3)_3$) in GP-DR@CTAB indicates the incorporation of nitrogen atoms through the doping of quaternary ammonium from CTAB. These findings are consistent with the head group of the CTAB surfactant.[38] Additionally, the presence of bromine (Br 3d) suggests that bromine atoms are primarily present in GP-DR@CTAB as part of the CTAB head group.[39] To gain a deeper understanding of the structural and chemical functionalities of GP-DR and GP-DR@CTAB, FTIR analyses were performed, as depicted in Fig. 2c. The band centered at 789 cm^{-1} is associated with quartz Si–O bond vibrations.[23,40] Intense bands within the range of 852–1283 cm^{-1} are attributed to the vibration mode of Si–O–T bonds (T represents tetrahedral Si or Al). The changing position of 1061 cm^{-1} (DR) to 1035 and 1020 cm^{-1} in alkali-activated GP-DR and GP-DR@CTAB, respectively, indicates successful activation of the diatomite raw rock (DR) with the alkaline activation solution and the resulting alkali-activated matrix.[26] In the case of GP-DR@CTAB, which includes CTAB surfactant, new vibrational bands appear at 1471, 2852, and 2924 cm^{-1}, corresponding to the bending vibrations of the CTAB surfactant incorporated into the alkali-activated matrix, confirming its presence in the alkali-activated matrix.[31] The results obtained from FTIR and XPS analyses provide consistent evidence for the presence of CTAB within the alkali-activated matrix.

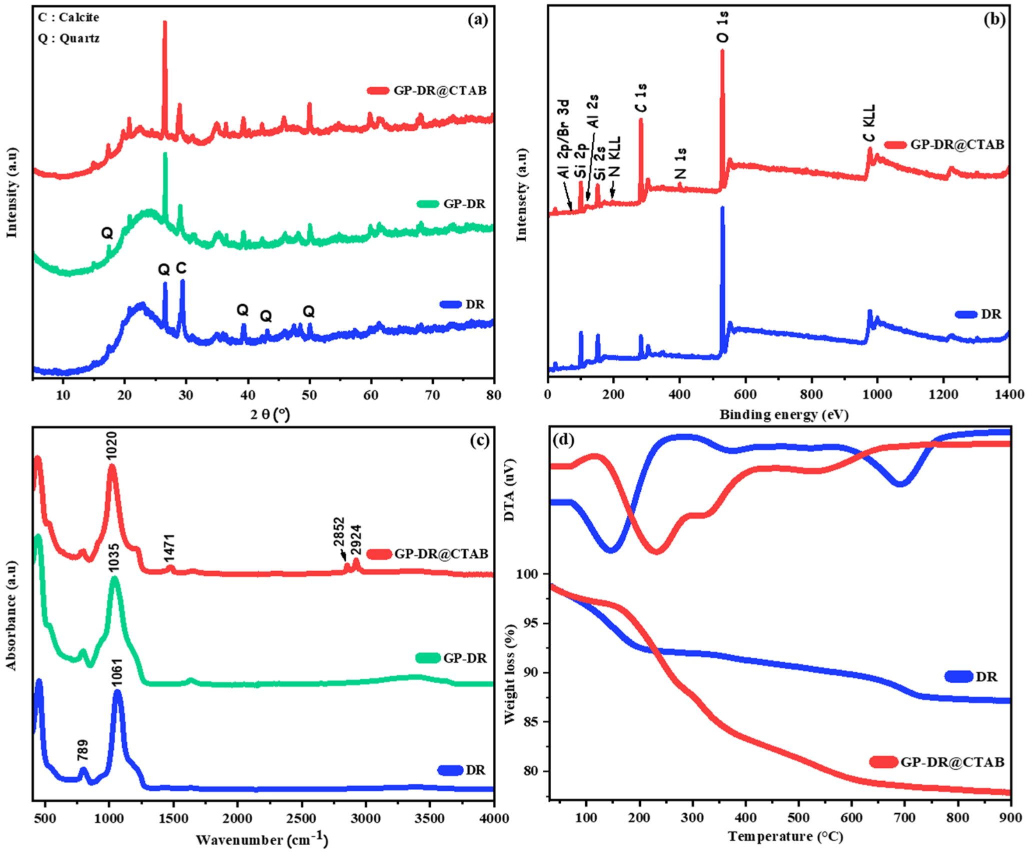

Fig. 2 (a) XRD data, (b) XPS survey spectrum, (c) FTIR spectra, and (d) TGA/DTA curves of DR, GP-DR and GP-DR@CTAB.

Fig. 2d illustrates the thermograms of thermal gravimetric and differential thermal analysis results obtained from the initial DR and GP-DR@CTAB, varying with the heating temperature. The TG thermogram of the DR demonstrates a weight loss phenomenon in the temperature range of 84–220 °C, resulting in a 6.77% reduction in weight. This loss can be attributed to the elimination of surface water, followed by the removal of fixed water or crystalline structure dihydroxylation.[41,42] Additionally, a prominent endothermic peak is observed between 563–851 °C, corresponding to the breakdown of calcite minerals and resulting in a weight loss of 2.85%.[43] GP-DR@CTAB displays two distinct weight losses above 150 °C. The thermal gravimetric (TG) curve indicates an approximately 11% weight loss between 150 and 300 °C, attributed to the degradation of the cationic surfactant adsorbed on the surface of the DR. Furthermore, a weight loss of approximately 6% occurs between 300 and 460 °C, indicating the degradation of the cationic surfactant within the layers of the DR.[44,45] The prepared GP-DR@CTAB sample demonstrates a notable increase in the mass loss of physisorbed water, suggesting an improvement in essential properties such as porosity.[23]

Fig. 3 presents the N_2 adsorption/desorption isotherms and the size distribution, both obtained using the BJH method, for two different samples: DR and GP-DR@CTAB. Both samples exhibit hysteresis loops type IV (Fig. 3a), indicating the existence of mesoporous characteristics according to the IUPAC. The specific surface area (S_{BET}), microporous volume (V_{mic}), mesoporous volume (V_{mes}), macroporous volume (V_{mac}), and total pore volume (V_{T}) values for DR and GP-DR@CTAB are provided in Table 1. The DR demonstrates a mesoporous nature, which is further confirmed by the BJH curves in Fig. 3b, showing specific surface area and total pore volume values of 15.92 $m^2 g^{-1}$ and 0.0749 $cm^3 g^{-1}$, respectively. In contrast, the GP-DR@CTAB sample, prepared with CTAB, exhibits the presence of mesopores and macropores, with specific surface area and pore volume values of 107.13 $m^2 g^{-1}$ and 0.7899 $cm^3 g^{-1}$, respectively. Notably, the porous alkali-activated prepared with CTAB surfactant shows a significant enhancement in porosity, approximately six times higher than that of diatomite raw rock (DR).

Furthermore, all samples demonstrate a maximum pore width ranging from 3 to 5 nm. Remarkably, GP-DR@CTAB presents an additional set of macropores with widths between 50 and 90 nm. This unusual occurrence of larger macropores was also observed in previous studies that utilized agents promoting mesoporosity in alkali-activated materials. These findings indicate that our obtained alkali-activated material possesses a more homogeneous distribution of mesopore and macropore diameters.

The morphologies of the DR and GP-DR@CTAB were studied by SEM and TEM image analysis (Fig. 4 and 5). Fig. 4a–c show characteristic morphologies of the DR revealing its unique disc-shaped structure with numerous mesopores and macropores

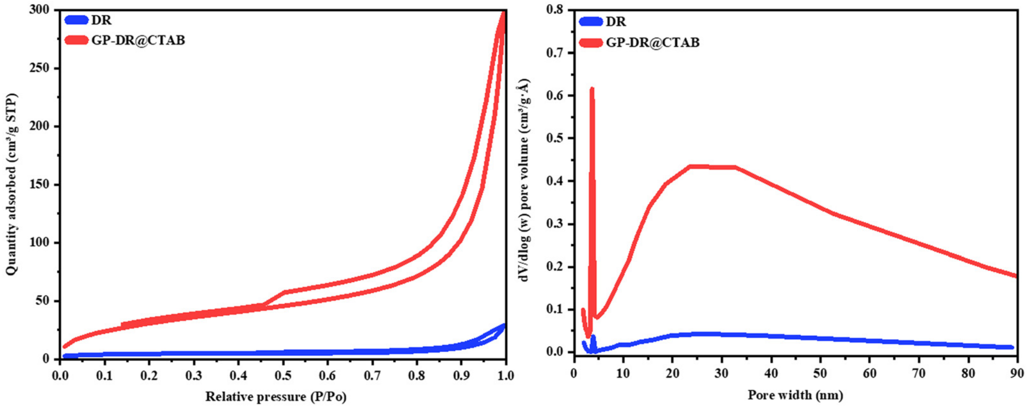

Fig. 3 Isotherms (left), pore volume (right) of DR and GP-DR@CTAB.

Table 1 Textural properties of DR and GP-DR@CTAB

	S_{BET} ($\mathrm{m^2\ g^{-1}}$)	V_{mic} ($\mathrm{cm^3\ g^{-1}}$)	V_{mes} ($\mathrm{cm^3\ g^{-1}}$)	V_{mac} ($\mathrm{cm^3\ g^{-1}}$)	V_{T} ($\mathrm{cm^3\ g^{-1}}$)
DR	015 ± 0.367	0.0015	0.0448	0.0286	0.0749
GP-DR@CTAB	107 ± 0.625	—	0.4637	0.3262	0.7899

spread throughout the central and peripheral regions.[46] This inherent porous network within diatomite contributes valuable properties to the alkali-activated composite. On the other hand, Fig. 4d–f depict the morphologies of the GP-DR@CTAB sample surface, showcasing an abundance of pores arranged in a regular manner. These images demonstrate the significant influence of diatomite's porous frustules in controlling pore orientation during the geopolymerization process. TEM results show that the DR (Fig. 5a–c) has discrete spherical pores with diameters ranging from around 230 nm, as observed. These results are in good agreement with the SEM analyses. After undergoing the geopolymerization process, the GP-DR@CTAB (Fig. 5d–f) images reaffirm the earlier description of its remarkably porous structure, characterized by a plethora of randomly dispersed nanopores throughout its composition.[47]

3.2. Adsorption test

In this study, Orange G (OG) dye was selected as the model organic pollutant dye. To identify the optimal conditions for the removal of Orange G using GP-DR@CTAB, we investigated different factors influencing the efficiency of the dye adsorption process, such as adsorbent dose, contact time, starting pH, and initial dye concentration. All adsorption experiments were performed in triplicate to ensure the reliability of the results. The adsorption kinetics were examined to clarify the underlying adsorption mechanism, while several physical models were assessed to provide deeper insight into the interactions between the GP-DR@CTAB adsorbent and OG adsorbate. The effects of each process parameter were discussed in more detail in the following section. The concentration of Orange G dye was measured using a JENWAY UV-Visible spectrophotometer (model 6705) at a wavelength of 478 nm.

3.2.1. Effect of dose, time, pH and concentration on OG dye in samples. To investigate the effect of adsorbent dose on the adsorption of OG, a range of 0.01 to 0.06 g $\mathrm{L^{-1}}$ for two samples, DR and GP-DR@CTAB, was tested, as shown in Fig. 6a. This experiment was realized in the following

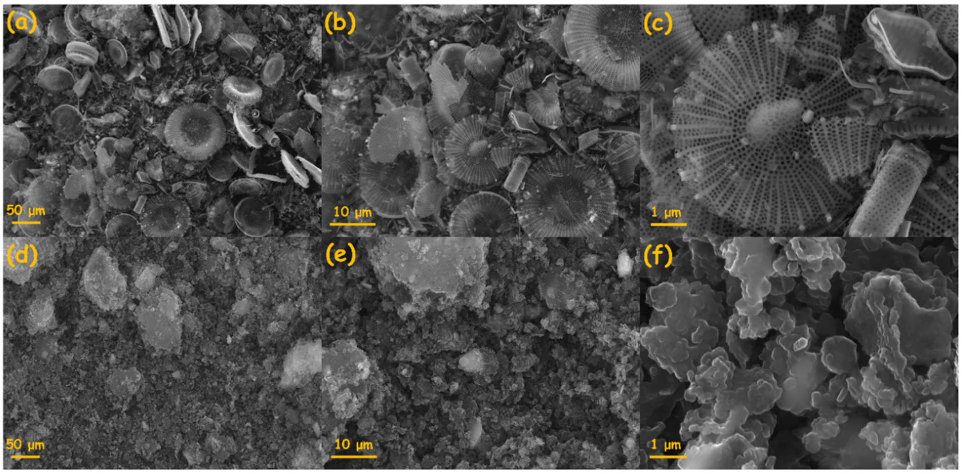

Fig. 4 SEM micrographs of DR (a)–(c), and GP-DR@CTAB (d)–(f).

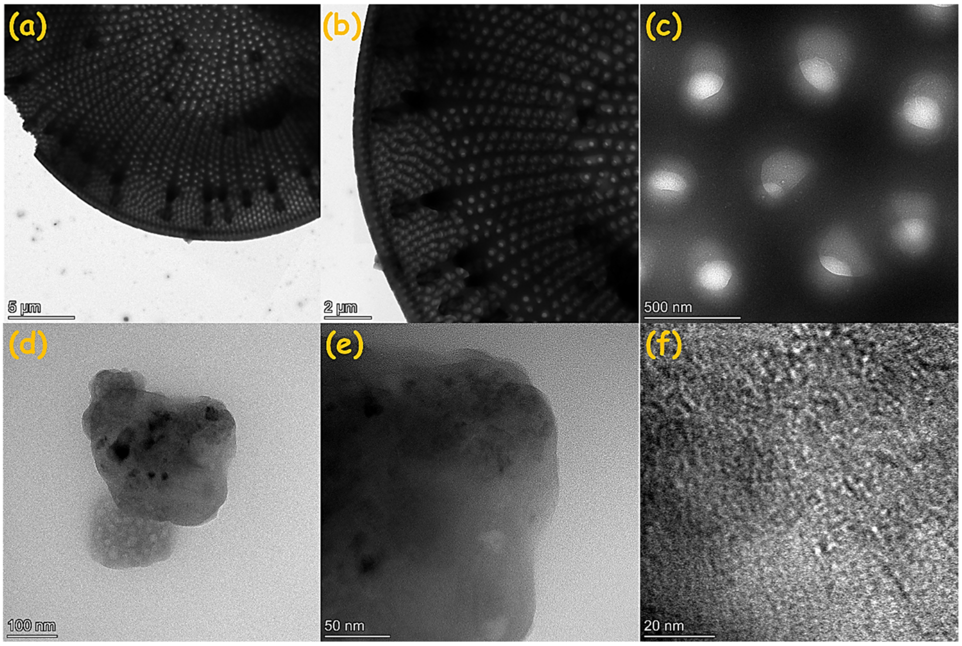

Fig. 5 TEM images of DR (a)–(c), and GP-DR@CTAB (d)–(f).

conditions: stirring time = 180 min, [OG] = 75 mg L^{-1}, temperature = 25 °C and pH = 6. The results indicate that the adsorption of OG increases with increasing concentrations of both adsorbents; however, DR and GP-DR@CTAB samples exhibited optimal OG removal efficiencies of 22% and 94%, respectively, achieved at adsorbent dosages of 0.01 g L^{-1} and 0.03 g L^{-1}, respectively. This behavior may be attributed to the greater availability of active sites at higher adsorbent doses, along with potential agglomeration of the adsorbent. Previous studies have also reported similar behavior, where increasing the dosage of CTAB-functionalized adsorbent correspondingly enhanced the removal rate of anionic dyes.[32]

The effect of contact time on the removal efficiency of OG was investigated using the following conditions: [DR] = 0.01 g L^{-1}, [GP-DR@CTAB] = 0.03 g L^{-1}, [OG] = 75 mg L^{-1}, temperature = 25 °C and pH = 6 (Fig. 6b). Initially, the retention of OG by DR is slow, whereas for the GP-DR@CTAB sample, the adsorption occurs more rapidly, attributed to its larger surface area and numerous active sites and active functional groups. Over time, the adsorption rate gradually decreases until saturation is achieved. The results indicate that maximum OG removal is achieved after an optimal contact time of 90 minutes for DR and 120 minutes for GP-DR@CTAB. After the adsorption process, the removal of OG is primarily controlled by the rate at which the dye transfers from the solution into the internal pores.

The pH of the solution plays a critical role in controlling the adsorption of dye onto the surface of the samples. The pH adjustments were carried out using 0.1 M hydrochloric acid (HCl) for acidification and 0.1 M sodium hydroxide (NaOH) for alkalization. The effect of pH on OG adsorption was investigated over a range of 2 to 10 and under controlled conditions: [DR] = 0.01 g L^{-1}, [GP-DR@CTAB] = 0.03 g L^{-1}, [OG] = 75 mg L^{-1}, stirring time (DR) = 90 min, stirring time (GP-DR@CTAB) = 120 min, temperature = 25 °C, the results are shown in Fig. 6c. It can be observed that a higher removal percentage of OG dye occurs in an acidic environment, with maximum adsorption efficiencies of 23% and 99% for DR and GP-DR@CTAB, respectively, at pH 2. Furthermore, the adsorption efficiency of both DR and GP-DR@CTAB remains relatively stable within the pH range of 2 to 6, showing only a slight decrease of 2% for each sample. This stability can be explained by the development of a positive net charge on the adsorbents. Consequently, the enhanced removal of OG dye at low pH values can be attributed to electrostatic attraction between the negatively charged functional groups of OG and the positively charged surfaces of GP-DR@CTAB. This observation is supported by Dong *et al.*,[48] whose study also demonstrated that, at low pH, protonation of the adsorbent enhances anionic dye adsorption through electrostatic interactions. Conversely, when the pH increases from 6 to 10, the adsorption efficiency decreases significantly by 12% for DR and 43% for GP-DR@CTAB. This reduction can be attributed to the development of negatively charged surfaces on both DR and GP-DR@CTAB, leading to electrostatic repulsion between the adsorbents and the negatively charged OG molecules.

To investigate the effect of initial OG concentration on the adsorption capacity of DR and GP-DR@CTAB, a series of solutions with concentrations ranging from 25 to 150 mg L^{-1} was prepared. The experiments were conducted under optimal conditions: [DR] = 0.01 g L^{-1}, [GP-DR@CTAB] = 0.03 g L^{-1}, stirring time of 90 minutes for DR and 120 minutes for GP-DR@CTAB, temperature = 25 °C, and pH = 6. As shown in Fig. 6d, the adsorption capacity of OG decreases with increasing initial OG concentration, reaching maximum values of 11 mg g^{-1} for DR and 44 mg g^{-1} for GP-DR@CTAB. The higher

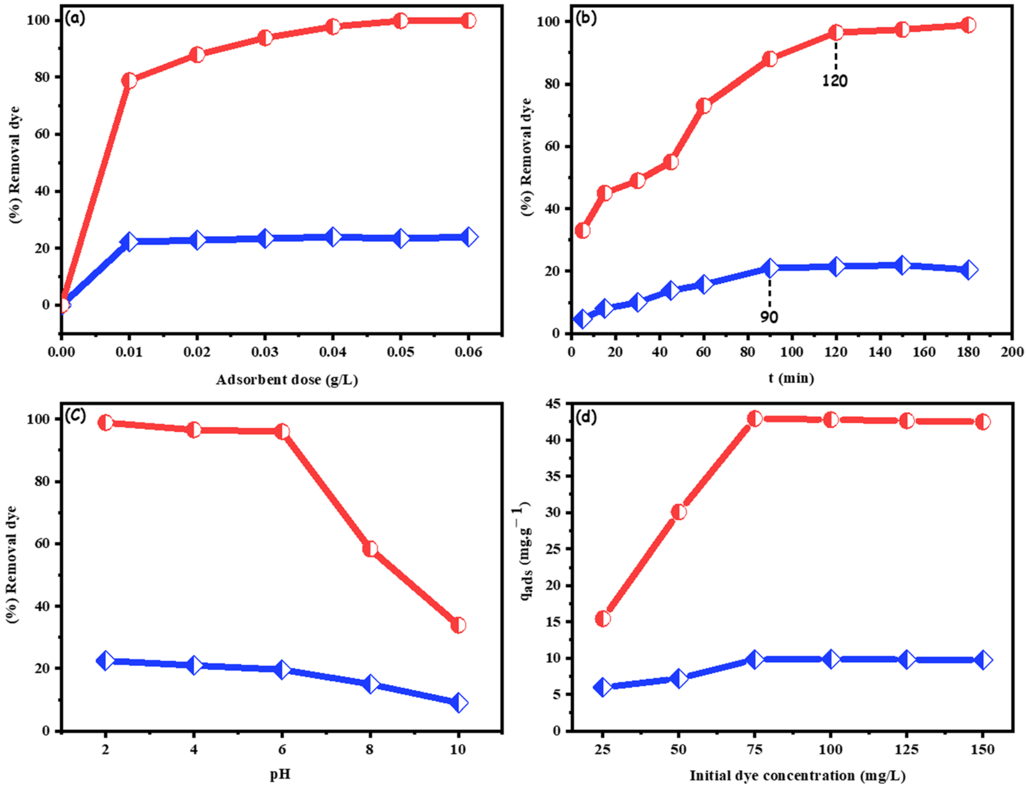

Fig. 6 Factors influencing the efficiency of the OG dye adsorption process, (a) adsorbent dose, (b) contact time, (c) starting pH, and (d) initial dye concentration of DR (blue curve), and GP-DR@CTAB (red curve).

adsorption at lower initial concentrations can be attributed to the greater availability of active sites on GP-DR@CTAB. Similar trends have been reported in the literature.[49] Over time, as these active sites become occupied, the number of available sites decreases, leading to reduced adsorption due to competition among sorbate molecules.

3.2.2. Adsorption kinetics. In order to investigate the adsorption processes of Orange G dye, two kinetic models were used, including pseudo first order and pseudo second order. The linear form of models are presented in eqn (1) and (2), respectively. Table 2 provides a summary of the characteristic parameters calculated for the two kinetic models.

$$\mathrm{Log}(q_\mathrm{e} - q_\mathrm{t}) = \mathrm{Log}\, q_\mathrm{e} - \frac{K_1}{2.303}\, t \qquad (1)$$

Table 2 Kinetics parameters obtained from pseudo first order model and pseudo second order model

Models	Parameters	DR	GP-DR@CTAB
Pseudo first order	R^2	0.9805	0.9892
	K_1 (min^{-1})	0.006	0.007
	q_e (mg g^{-1})	10.23 ± 1	26.25 ± 1
	$q_\mathrm{e}^{\mathrm{exp}}$ (mg g^{-1})	07.19 ± 1	30.07 ± 2
Pseudo second order	R^2	0.9901	0.9993
	K_2 (g mg^{-1} min^{-1})	0.003	0.003
	q_e (mg g^{-1})	08.57 ± 2	32.05 ± 1
	$q_\mathrm{e}^{\mathrm{exp}}$ (mg g^{-1})	07.19 ± 1	30.07± 2

$$\frac{t}{q_\mathrm{t}} = \frac{1}{K_2 q_\mathrm{e}^2} + \frac{1}{q_\mathrm{e}}\, t \qquad (2)$$

K_1 (min^{-1}) and K_2 (g mg^{-1} min^{-1}) are the pseudo first order and pseudo second order kinetic constants respectively.

According to the results of Table 2, the values of the correlation coefficients of the pseudo second order kinetic model are almost equal to 1 compared to the other model. In addition, the values of the absorbed quantities calculated q_e by this model are almost identical to the experimental ones $q_\mathrm{e}^{\mathrm{exp}}$ of treated OG dye. According to the kinetic study of the adsorption of pollutant in contact with our materials using different kinetic models, the results indicated that the adsorption process could be described by the pseudo second order model.[50] This model assumes that the rate-limiting step in the adsorption process is a chemical sorption, which involves electron exchanges at the solid–liquid interface.[51]

3.2.3. Adsorption models. In order to determine the adsorption capacity of the OG dye on the adsorbents and the type of adsorption mechanism, we used two types of isotherms (Langmuir and Freundlich models). The classical Langmuir and Freundlich models characterizing the formation of a monolayer will be used for their simplicity of implementation.

To study the adsorption isotherms of OG by DR and GP-DR@CTAB, volumes of 25 mL with concentration (75 mg L^{-1})

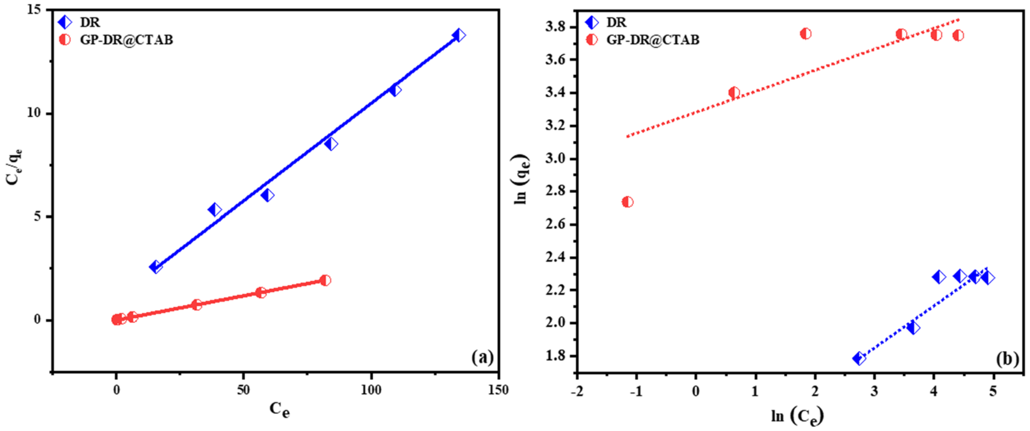

Fig. 7 (a) Langmuir isotherms, (b) Freundlich isotherms for the adsorption of OG.

of OG are brought into contact with a mass of 0.02 g L^{-1} of the adsorbent. The experimental conditions are analogous to those of the adsorption kinetics (Fig. 7).

The Langmuir isotherm is one of the models, which is based on the absence of interactions between entities adsorbed on sites of the same nature. This model assumes a homogeneous adsorption surface with binding sites having equal energies. The linear equation of the Langmuir isotherm can be expressed as follows:[52]

$$\frac{C_e}{q_e} = \frac{C_e}{q_m} + \frac{1}{K_L q_m} \quad (3)$$

with, K_L is the Langmuir constant; q_{max} (mg g^{-1}) represents the maximum adsorption capacity under the experimental conditions. q_m and K_L are determined from the plot of C_e/q_e as a function of C_e.

The Freundlich isotherm is an empirical equation based on an exponential distribution of adsorption sites and energies. The linear equation of Freundlich is represented as follows:[3]

$$\ln(q_e) = \ln(K_F) + \frac{1}{n}\ln(C_e) \quad (4)$$

with: K_F is the Freundlich constant linked to the binding energy. n is the heterogeneity factor. K_F and n are determined from the plot of ln (q_e) as a function of ln (C_e).

The values of the constants of each model (Table 3), indicate that the Langmuir model perfectly describes the adsorption process of orange G in the presence of two materials (DR and GP-DR@CTAB), with correlation coefficient values almost equal to 1. The maximum adsorbed quantities obtained by the Langmuir model in the presence of the DR and GP-DR@CTAB materials are very close to those obtained experimentally 9.81 mg g^{-1} and 42.48 mg g^{-1}. This confirms the validity of the Langmuir model, which is based on the absence of interactions between entities adsorbed on sites of the same nature.[50]

Table 3 Isotherms parameters for the adsorption of OG

Isotherm models	Parameters	DR	GP-DR@CTAB
Langmuir	R^2	0.9888	0.9999
	K_L (L mg^{-1})	2.077	2.721
	q_m (mg g^{-1})	10.65 ± 1	42.74 ± 2
	q_e^{exp} (mg g^{-1})	9.81± 2	42.48 ± 3
Freundlich	R^2	0.8641	0.7805
	K_F ($mg^{1-1/n}$ g^{-1} $L^{1/n}$)	3.047	23.34
	n	3.953	6.25

To assess the efficiency of our adsorbent in removing Orange G (OG), we compared its performance with values reported for other adsorbents in the literature (Table 4). According to Table 5, these studies have been summarized and compared based on the characteristics of geopolymers and dyes. The table highlights the results of several recent investigations focused on the removal of Orange G (OG). While some literature reports demonstrate high adsorption capacities and removal efficiencies for anionic dyes, their practical application is often limited by complex preparation procedures and the requirement for strongly acidic conditions, which pose environmental and economic challenges. In contrast, the synthesis process in our study is designed to be environmentally friendly, utilizing a simple modification method under mild conditions without the use of toxic chemicals or high energy consumption. Diatomite, a naturally abundant and low-cost material, further minimizes the environmental footprint. Our approach involves a straightforward preparation of CTAB-modified, diatomite-based alkali-activated materials under spontaneous conditions. The use of readily available diatomite not only reduces production costs but also enhances the environmental sustainability of the process. These advantages make our method more practical, cost-effective, and sustainable compared to existing approaches reported in the literature.

3.2.4. Thermodynamics study.

To understand the interaction between adsorbent–adsorbate, the Thermodynamic parameters, namely Gibbs free energy (ΔG°), entropy change (ΔS°), and enthalpy change (ΔH°), were calculated at 298 K, 323 K, 348 K and 373 K using van't Hoff plots according to the followings equations (eqn (5)–(7)):[64]

$$\Delta G^\circ = -RT\ln K_d \quad (5)$$

$$\Delta G^0 = \Delta H^0 - T\Delta S^0 \quad (6)$$

Table 4 Assessment of OG adsorption capacities on diverse adsorbent materials

Adsorbent	Q_{max} (mg g^{-1})	Adsorbent dosage (g L^{-1})	pH	[OG] (mg L^{-1})	Kinetic model	Isotherm model	Ref.
Ungrafted chitosan	34	3	7	300	PSO	L	53
Modified sawdust	5.48	20	2	50	PFO	L	54
Modified wheat husk	31.25	2.5	2	10	PSO	F	55
Co_3O_4	33.3	1	2	50	PSO	L	56
Modified rice husk char	38.8	2	4	50	PSO	L	57
Magnetic graphene oxide	20.85	1	6	60	PSO	L	58
Bagasse fly ash	18.8	2	4	10	PSO	F	59
Modified formaldehyde	14.1	0.1	4	60	PSO	L	60
Cerium dioxide	33.33	2	2	15	PSO	L	61
ODA nano-clay	39.4	1	8	50	PSO	—	62
Magnetic biochar	32.36	5	7	30	PSO	L	63
GP-DR@CTAB	42.74	0.02	6	75	PSO	L	This work

Keys: L = Langmuir, F = Freundlich, PFO = Pseudo first order, PSO = Pseudo second order.

Table 5 van't Hoff plot of thermodynamic factors

Thermodynamic parameters						
	$\Delta G°$ (kJ mol^{-1})				$\Delta H°$ (kJ mol^{-1})	$\Delta S°$ (kJ mol^{-1} K^{-1})
T (K)	298	308	318	328		
DR	−2.22	−3.21	−4.65	−6.95	44.17	0.151
GP-DR@CTAB	−13.37	−14.71	−14.96	−15.82	80.82	0.081

$$\ln K_d = -\frac{\Delta H°}{RT} + \frac{\Delta S°}{R} \quad (7)$$

where: K_d is the equilibrium constant, R is the ideal gas constant (8.314 J K^{-1} mol^{-1}) and T is the temperature (K).

Fig. 8a illustrates the adsorption of OG molecules onto DR and GP-DR@CTAB at different temperatures. Thermodynamic parameters, including Gibbs free energy ($\Delta G°$), entropy change ($\Delta S°$), and enthalpy change ($\Delta H°$), were determined at 293 K, 303 K, and 313 K using van't Hoff plots (Fig. 8b) and are summarized in Table 5. The adsorption curve for GP-DR@CTAB shows minimal temperature dependence (+3 mg g^{-1}), likely due to physisorption mechanisms such as electrostatic attractions and hydrophobic interactions, which are generally less sensitive to temperature variations. This aligns with previous findings by Ettahiri *et al.*[34] The negative $\Delta G°$ values confirm the spontaneity of OG adsorption onto DR and GP-DR@CTAB. Additionally, the positive $\Delta H°$ values indicate that the process is endothermic, while the positive $\Delta S°$ values suggest increased randomness at the adsorbent–adsorbate interface during adsorption.

3.2.5. Proposed mechanism of OG adsorption onto GP-DR@CTAB. The adsorption of OG onto GP-DR@CTAB involves several key interaction mechanisms, as shown in Fig. 9. The negatively charged sites on the alkali activated matrix, primarily due to the aluminum (Al) atoms, attract the positively charged head group (quaternary ammonium, N^+) of CTAB molecules through electrostatic interactions. This creates a hydrophobic surface as the hydrocarbon tails of CTAB extend outward, allowing for significant hydrophobic interaction between the CTAB tails and the aromatic rings of OG, particularly the naphthalene ring. Additionally, the sulfonate groups ($-SO_3^-$) on OG strongly interact with the positively charged headgroups of CTAB, resulting in strong electrostatic attraction. This electrostatic interaction further enhances the adsorption of Orange G onto the surface. Moreover, hydrogen bonding occurs between the oxygen-containing sulfonate groups

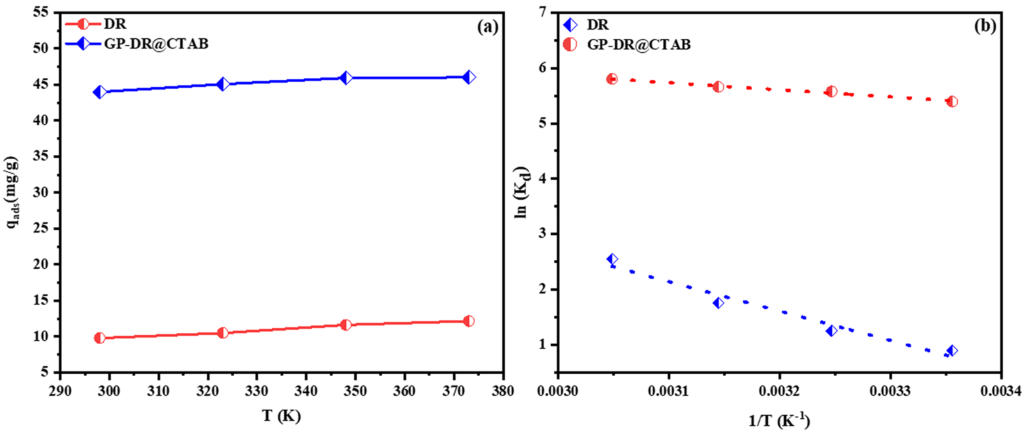

Fig. 8 (a) Temperature effect for the adsorption of OG, (b) van't Hoff plot ([DR] = 0.01 g L^{-1}, [GP-DR@CTAB] = 0.03 g L^{-1}, [OG] = 75 mg g^{-1}, stirring time of 90 minutes for DR and 120 minutes for GP-DR@CTAB, and pH = 6.

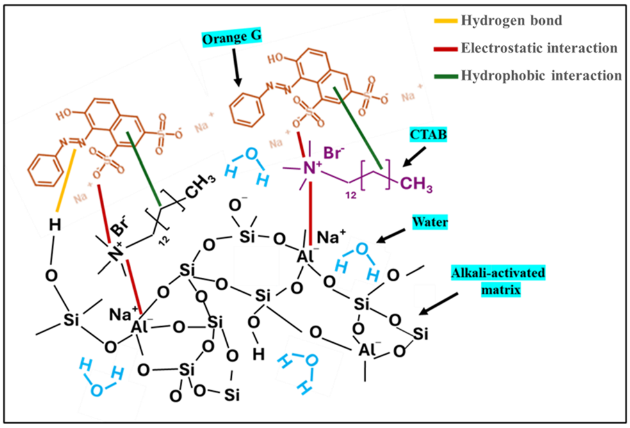

Fig. 9 Adsorption mechanism for OG removal by GP-DR@CTAB.

on OG and the hydroxyl groups (–OH) present on the alkali-activated surface, contributing further to the stabilization of the adsorbed dye molecules. These combined effects hydrophobic interactions, electrostatic attraction, and hydrogen bonding synergistically result in a highly efficient adsorption of OG onto CTAB-modified alkali-activated. This mechanism is consistent with the work of Qian Li *et al.*,[50] which demonstrated that the adsorption of the pertechnetate anion (ReO_4^-) onto CTAB@MGMs begins with Br^- dissociation, facilitating the electrostatic interaction between ReO_4^- and the positively charged N^+. The ReO_4^- subsequently forms an insoluble CTAB–ReO_4 complex, which is immobilized on the CTAB@MGMs, effectively removing ReO_4^- from the solution. Açışlı *et al.* similarly used CTAB to modify a fly ash-based geopolymer for capturing the anionic dye Acid Blue 185, where the adsorption mechanism was driven by electrostatic interactions rather than surface or pore characteristics.[32]

3.2.6. Limitations, challenges, and future research recommendations. GP-DR@CTAB hold significant potential for the effective removal of organic pollutants like Orange G from contaminated water. However, their practical application faces certain limitations and challenges. Moreover, the selectivity of GP-DR@CTAB in the presence of competing ions commonly found in real wastewater, such as chloride, nitrate, sulfate, calcium, and magnesium, was not assessed in this study and represents an important area for further investigation. Additionally, while the material demonstrates promising adsorption capacity, challenges related to its regeneration and reusability could impact long-term performance and economic viability. These challenges include mass loss during the recycling process and difficulties in recovering the adsorbent from the solution, as it tends to collect on the support material, making its retrieval complex. To address these concerns, future research should focus on enhancing material stability through surface modifications or composite formation with nanoparticles. Furthermore, integrating the adsorbent into stable matrices, such as encapsulating it within polymer beads like alginate or utilizing innovative approaches like 3D printing, which has recently been explored in the field of alkali-activated materials, could help minimize mass loss during recycling and enhance its handling in aqueous environments. By improving recovery and reuse, these strategies are expected to reduce replacement costs and maintain the adsorbent's cost-effectiveness over multiple cycles, supporting its practical economic viability. This strategy would also improve the material's stability and facilitate easier recovery for reuse. Additionally, while CTAB modification effectively enhances the material's adsorption performance for anionic dyes like Orange G, it should be acknowledged that CTAB is a quaternary ammonium surfactant with known toxicity to aquatic life. Consequently, the potential leaching of residual CTAB could pose environmental risks if not adequately controlled. To address this concern, future studies should include systematic leachability assessments by soaking the adsorbent in deionized water under representative conditions and analyzing the leachate for residual surfactant, for example, by bromide ion detection or total organic carbon (TOC) measurement. If measurable CTAB leaching is observed, additional washing steps or mild thermal treatments should be considered to further reduce residual surfactant content. This approach will help ensure that the adsorbent's enhanced removal performance does not compromise its environmental safety, thereby supporting its sustainable application in water treatment. Moreover, it is recommended that future research includes surface charge characterization, such as zeta potential measurements, for the diatomite rock and the alkali-activated diatomite before and after CTAB modification. This would confirm the expected negative surface charge after activation and the charge reversal or reduction in negative charge due to CTAB adsorption, which is crucial for understanding and optimizing electrostatic interactions with anionic pollutants like Orange G. Additionally, a life cycle assessment could be conducted to evaluate the environmental impact and long-term sustainability of the adsorbent.

4. Conclusion

This study examines the adsorption properties of CTAB-modified diatomite-based alkali-activated for the removal of Orange G (OG). XRD demonstrated successful geopolymerization, while FTIR and XPS analyses verified the integration of CTAB into the alkali-activated structure. The TGA/DTA showed increased mass loss of physisorbed water in GP-DR@CTAB compared to unmodified diatomite, highlighting improved porosity and permeability. BET analysis further confirmed a high surface area of 107.13 $m^2\ g^{-1}$, with diatomite's porous frustules playing a critical role in controlling pore orientation during synthesis. Adsorption experiments revealed that the process followed a pseudo-second-order kinetic model, with the Langmuir isotherm providing the best fit and a maximum adsorption capacity of 42.74 $mg\ g^{-1}$. The primary adsorption mechanism was identified as physical adsorption driven by electrostatic attraction between OG and GP-DR@CTAB. These results suggest that GP-DR@CTAB is a low-cost, eco-friendly adsorbent with potential applications, offering superior performance compared to other materials reported in the literature.

Conflicts of interest

The authors declare that they have no known competing financial interests or personal relationships that could have appeared to influence the work reported in this paper.

Data availability

Data will be made available on request.

References

1 J. R. Martins, R. M. N. D. Hotza and J. A. L. L. Senff, Waste -Derived Geopolymers for Artificial Coral Development by 3D Printing, *J. Sustain. Metall.*, 2025, **11**, 114–125, DOI: **10.1007/s40831-025-01016-3**.

2 K. Fritah, M. Khachane, A. Bouddouch and B. Akhsassi, New insight for enhanced photocatalytic activity of $Bi_{4-x}La_xTi_3O_{12}$ $(0 \leq x \leq 1)$ solid solution: A case study on degradation of Rhodamine B under UV light irradiation, *Opt. Mater.*, 2024, **150**, 115182, DOI: **10.1016/j.optmat.2024.115182**.

3 A. Chaoui, S. Farsad, A. Ben Hamou, A. Amjlef, N. Nouj, M. Ezzahery and N. El Alem, Reshaping environmental sustainability: Poultry by-products digestate valorization for enhanced biochar performance in methylene blue removal, *J. Environ. Manage.*, 2024, **351**, 119870, DOI: **10.1016/j.jenvman.2023.119870**.

4 N. Iberache, F. E. Titchou, M. Errami, S. Ben-Aazza, A. Driouiche, R. A. Akbour, M. Hamdani and A. Hadfi, Removal of the Insecticide Imidacloprid from Water in Commercial Formulation using Electro-Fenton and Photo-Electro-Fenton: Optimization of COD Removal through Response Surface Methodology RSM-CCD, *Chem. Eng. Process.*, 2024, **196**, 109633, DOI: **10.1016/j.cep.2023.109633**.

5 M. El Fazdoune, N. K. Bakirhan, K. Bahend, E. A. Bazzaoui and M. Bazzaoui, MWCNT-PMB Modified Electrode for Enhanced Detection of Methiocarb Insecticide, *J. Electrochem. Soc.*, 2025, **172**, 017509, DOI: **10.1149/1945-7111/ada586**.

6 Y. Ettahiri, L. Bouna, A. Brahim, A. Benlhachemi, B. Bakiz, D. Eliche-quesada, P. Luis, B. Bakiz and J. S. Pedro, Synthesis and characterization of porous and photocatalytic geopolymers based on natural clay: Enhanced properties and efficient Rhodamine B decomposition, *Appl. Mater. Today*, 2024, **36**, 102048, DOI: **10.1016/j.apmt.2023.102048**.

7 B. Akhsassi, Y. Ettahiri, B. Bakiz, A. Taoufyq, S. Villain, C. Favotto, F. Guinneton, J. Gavarri and A. Benlhachemi, Novel Z-scheme Bi3O4Cl/Bi24O31Cl10 2D/3D heterojunction for enhanced photocatalytic activity under visible light, *Colloids Surf., A*, 2023, **673**, 131762, DOI: **10.1016/j.colsurfa.2023.131762**.

8 Z. Huo, B. Akhsassi, J. Yu, M. Zheng, T. Lan, Q. He, C. Boudon, G. Xu, A. Proust, G. Izzet and L. Ruhlmann, Photocatalytic Recovery of Noble Metals by Covalent Silyl Polyoxophosphotungstate-Porphyrin Copolymers, *Inorg. Chem.*, 2025, 3371–3383, DOI: **10.1021/acs.inorgchem.4c04890**.

9 A. Imgharn, M. Laabd, Y. Naciri, A. Hsini, F. Z. Mahir, H. Zouggari and A. Albourine, Insights into the performance and mechanism of PANI@Hydroxapatite-Montmorillonite for hexavalent chromium Cr (VI) detoxification, *Surf. Interfaces*, 2023, **36**, 102568, DOI: **10.1016/j.surfin.2022.102568**.

10 M. T. Yagub, T. K. Sen, S. Afroze and H. M. Ang, Dye and its removal from aqueous solution by adsorption: a review, *Adv. Colloid Interface Sci.*, 2014, **209**, 172–184, DOI: **10.1155/2022/4551212**.

11 M. M. Almeida, N. P. F. Gonçalves, T. Gameiro, Z. Alves, J. A. Labrincha and R. M. Novais, 3D-printing bauxite residue/fly ash-containing geopolymers as promising metal sorbents for water treatment, *Waste Manage.*, 2024, **190**, 35–44, DOI: **10.1016/j.wasman.2024.09.007**.

12 A. Bouddouch, E. Amaterz, B. Bakiz, A. Taoufyq, F. Guinneton, S. Villain, J. R. Gavarri, J. C. Valmalette and A. Benlhachemi, Customized synthesis of functional bismuth phosphate using different methods: photocatalytic and photoluminescence properties enhancement, *Nanotechnol. Environ. Eng.*, 2021, **6**, 1–12, DOI: **10.1007/s41204-020-00097-7**.

13 A. Bouddouch, E. Amaterz, B. Bakiz, F. Guinneton, A. Taoufyq, S. Villain, J. R. Gavarri, M. Mansori, J. C. Valmalette and A. Benlhachemi, High photocatalytic performance of bismuth phosphate and corresponding photodegradation mechanism of Rhodamine B, *Res. Chem. Intermed.*, 2022, **48**, 3315–3334, DOI: **10.1007/S11164-022-04762-1**.

14 L. Mllaoiy, S. Bikerchalen, B. Akhsassi, O. Ouzaguine, B. Bakiz, S. Villain, A. Taoufyq, F. Guinneton, J. C. Valmalette, J. R. Gavarri and A. Benlhachemi, Engineering BiOBr nanoplatelets with $\{001\}$ facet exposure: Synthesis, characterization and visible-light photocatalytic properties, *Ceram. Int.*, 2025, **51**, 14807–14820, DOI: **10.1016/j.ceramint.2025.01.323**.

15 A. Ben Hamou, M. Enneiymy, S. Farsad, A. Amjlef, A. Chaoui, N. Nouj, A. Majdoub, A. Jada, M. Ez-Zahery and N. El Alem, Novel chemically reduced cobalt-doped g-C3N4 (CoCN-x) as a highly heterogeneous catalyst for the super-degradation of organic dyes *via* peroxymonosulfate activation, *Mater. Adv.*, 2024, **5**, 1960–1976, DOI: **10.1039/d3ma00818e**.

16 Y. Ettahiri, B. Akhsassi, M. El Fazdoune, A. Bouddouch, L. Bouna, A. Benlhachemi, L. Pérez-Villarejo and R. De Fátima Peralta Muniz Moreira, From synthesis to applications: A comprehensive review of geopolymer materials for photocatalytic degradation of organic pollutants, *Sep. Purif. Technol.*, 2024, **330**, 125396, DOI: **10.1016/j.seppur.2023.125396**.

17 A. Imgharn, T. Sun, J. Nicolle, Y. Naciri, A. Hsini, A. Albourine and C. Ania, A Simple Approach to Prepare a C3N4/MoO3 Heterojunction with Improved Photocatalytic Performance for the Degradation of Methylparaben, *Catalysts*, 2024, **14**, 170, DOI: **10.3390/catal14030170**.

18 R. M. Novais, G. Ascensão, D. M. Tobaldi, M. P. Seabra and J. A. Labrincha, Biomass fly ash geopolymer monoliths for effective methylene blue removal from wastewaters, *J. Cleaner Prod.*, 2018, **171**, 783–794, DOI: **10.1016/j.jclepro.2017.10.078**.

19 R. M. Novais, R. C. Pullar and J. A. Labrincha, Geopolymer foams: An overview of recent advancements, *Prog. Mater. Sci.*, 2020, **109**, 100621, DOI: **10.1016/J.PMATSCI.2019.100621**.

20 Z. Alves, J. Carvalheiras, L. Senff, A. M. Lacasta, I. R. Cantalapiedra, J. A. Labrincha and R. M. Novais, A comparison between the use of cork and synthetic aggregates in the production of geopolymer composites, *Constr. Build. Mater.*, 2024, **438**, 1–10, DOI: **10.1016/j.conbuildmat.2024.137147**.

21 L. Bouna, Y. Ettahiri, A. Elimbi, A. Benlhachemi and M. Cyr, Role of washing process in the improvement of surface properties of porous geopolymers, *J. Porous Mater.*, 2022, **31**, 569–576, DOI: **10.1007/s10934-023-01533-0**.

22 A. García-Díaz, P. Delgado-Plana, S. Bueno-Rodríguez and D. Eliche-Quesada, Investigation of waste clay brick (chamotte) addition and activator modulus in the properties of alkaline activation cements based on construction and demolition waste, *J. Build. Eng.*, 2024, **84**, 108568, DOI: **10.1016/j.jobe.2024.108568**.

23 L. Bouna, A. Ait El Fakir, A. Benlhachemi, K. Draoui, M. Ezahri, B. Bakiz, S. Villain, F. Guinneton and N. Elalem, Synthesis and characterization of mesoporous geopolymer based on Moroccan kaolinite rich clay, *Appl. Clay Sci.*, 2020, **196**, 105764, DOI: **10.1016/j.clay.2020.105764**.

24 V. F. F. Barbosa, K. J. D. MacKenzie and C. Thaumaturgo, Synthesis and characterisation of materials based on inorganic polymers of alumina and silica: Sodium polysialate polymers, *Int. J. Inorg. Mater.*, 2000, **2**, 309–317, DOI: **10.1016/S1466-6049(00)00041-6**.

25 M. A. Gómez-Casero, P. J. Sánchez-Soto, E. Castro and D. Eliche-Quesada, Effect of olive-pruning fibres as reinforcements of alkali-activated cements based on electric arc furnace slag and biomass bottom ash, *Arch. Civ. Mech. Eng.*, 2024, **24**, 1–20, DOI: **10.1007/s43452-024-00882-0**.

26 Y. Ettahiri, B. Bouargane, K. Fritah, B. Akhsassi, A. Aziz, L. Bouna, A. Benlhachemi and R. M. Novais, A state-of-the-art review of recent advances in porous geopolymer: Applications in adsorption of inorganic and organic contaminants in water, *Constr. Build. Mater.*, 2023, **395**, 119870, DOI: **10.1016/j.conbuildmat.2023.132269**.

27 K. S. Al-Thubaiti and Z. Khan, Cationic surfactant modified iron nanoparticles for removal of orange II in batch mode: Kinetics, isotherms, mechanistic, and thermodynamic approach, *Int. J. Chem. Kinet.*, 2024, **56**, 368–383, DOI: **10.1002/kin.21715**.

28 M. G. Murphy, M. Al-Khalidi, J. F. S. Crocker, S. H. Lee, P. O'Regan and P. D. Acott, Two formulations of the industrial surfactant, Toximul, differentially reduce mouse weight gain and hepatic glycogen *in vivo* during early development: Effects of exposure to Influenza B Virus, *Chemosphere*, 2005, **59**, 235–246, DOI: **10.1016/j.chemosphere.2004.11.084**.

29 D. V. Goia and E. Matijević, Tailoring the particle size of monodispersed colloidal gold, *Colloids Surf., A*, 1999, **146**, 139–152, DOI: **10.1016/S0927-7757(98)00790-0**.

30 O. M. Khabeeri, S. A. Al-Thabaiti and Z. Khan, Effects of ionic surfactants on the nucleation and growth of cyanidin 3,5-di-O-glucoside capped zerovalent iron nanoparticles, *Colloids Interface Sci. Commun.*, 2020, **37**, 100272, DOI: **10.1016/j.colcom.2020.100272**.

31 Z. Yu, W. Song, J. Li and Q. Li, Improved simultaneous adsorption of Cu(II) and Cr(VI) of organic modified metakaolin-based geopolymer, *Arab. J. Chem.*, 2020, **13**, 4811–4823, DOI: **10.1016/j.arabjc.2020.01.001**.

32 Ö. Açışlı, İ. Acar and A. Khataee, Preparation of a surface modified fly ash-based geopolymer for removal of an anionic dye: Parameters and adsorption mechanism, *Chemosphere*, 2022, **295**, 133870, DOI: **10.1016/j.chemosphere.2022.133870**.

33 Y. Ettahiri, A. Bouddouch, B. Akhsassi, A. Khali, L. Bouna, A. Benlhachemi and L. Pérez-Villarejo, Optimized porous alkali-activated material for superior dye removal: synthesis and performance analysis, *Mater. Adv.*, 2025, **6**, 2435–2447, DOI: **10.1039/d4ma01065e**.

34 Y. Ettahiri, L. Bouna, J. V. Hanna, A. Benlhachemi, H. L. Pilsworth, A. Bouddouch and B. Bakiz, Pyrophyllite clay-derived porous geopolymers for removal of methylene blue from aqueous solutions, *Mater. Chem. Phys.*, 2023, **296**, 127281, DOI: **10.1016/j.matchemphys.2022.127281**.

35 Y. Zeng, N. Duan, C. Fu, D. Liao, X. Song, S. Jin and K. Cui, Preparation and characterization of tungsten tailing-based geopolymers, *Ceram. Int.*, 2023, **49**, 22043–22053, DOI: **10.1016/J.CERAMINT.2023.04.030**.

36 L. M. Kljajević, S. S. Nenadović, M. T. Nenadović, N. K. Bundaleski, B. Todorović, V. B. Pavlović and Z. L. Rakočević, Structural and chemical properties of thermally treated geopolymer samples, *Ceram. Int.*, 2017, **43**, 6700–6708, DOI: **10.1016/J.CERAMINT.2017.02.066**.

37 Q. Wan, Y. Zhang and R. Zhang, Using mechanical activation of quartz to enhance the compressive strength of metakaolin based geopolymers, *Cem. Concr. Compos.*, 2020, **111**, 103635, DOI: **10.1016/J.CEMCONCOMP.2020.103635**.

38 N. A. Mahat, N. S. M. Nor and S. A. Shamsudin, Effects of Positive Carbon Quantum Dots on Gram-negative Bacteria as an Antimicrobial Agent, *J. Inorg. Organomet. Polym. Mater.*, 2022, **32**, 2428–2440, DOI: **10.1007/s10904-022-02314-z**.

39 S. Petlitckaia and A. Poulesquen, Design of lightweight metakaolin based geopolymer foamed with hydrogen peroxide, *Ceram. Int.*, 2019, **45**, 1322–1330, DOI: **10.1016/J.CERAMINT.2018.10.021**.

40 Y. Ettahiri, D. M. Samuel, L. Bouna, A. Khali, A. Aziz, A. Benlhachemi, L. Pérez-Villarejo and W. M. Kriven, Comparative study of physicochemical properties of geopolymers prepared by four Moroccan natural clays, *J. Build. Eng.*, 2023, **80**, 108021, DOI: **10.1016/j.jobe.2023.108021**.

41 S. Yusan, K. Korzhynbayeva, S. Aytas, S. Tazhibayeva and K. Musabekov, Preparation and investigation of structural properties of magnetic diatomite nanocomposites formed with different iron content, *J. Alloys Compd.*, 2014, **608**, 8–13, DOI: **10.1016/J.JALLCOM.2014.04.064**.

42 L. Bouna, A. A. El Fakir, Y. Ettahiri, H. Abara, A. Jada, K. Draoui, A. Benlhachemi and M. Ezahri, Understanding

the impact of kaolinite/muscovite ratio in natural clays on oxide contents, physisorbed water, and structural water fractions, *Mater. Chem. Phys.*, 2024, **314**, 128858, DOI: **10.1016/j.matchemphys.2023.128858**.

43 S. S. Ibrahim and A. Q. Selim, Heat Treatment of Natural Diatomite, *Physicochem. Probl. Miner. Process.*, 2012, **48**, 413–424, DOI: **10.5277/ppmp120208**.

44 G. Sui, Y. Zhao, Q. Zhang and Q. Fu, Enhanced mechanical properties of olefin block copolymer by adding a quaternary ammonium salt functionalized graphene oxide, *RSC Adv.*, 2016, **6**, 54785–54792, DOI: **10.1039/c6ra11451b**.

45 M. Guo, G. Yang, S. Zhang, Y. Zhang, C. Gao, C. Zhang and P. Zhang, Co-modification of Bentonite by CTAB and Silane and its Performance in Oil-Based Drilling Mud, *Clays Clay Miner.*, 2020, **68**, 646–655, DOI: **10.1007/s42860-020-00093-7**.

46 K. Felaous, A. Aziz and M. Achab, Physico-mechanical and durability properties of new eco-material based on blast furnace slag activated by Moroccan diatomite gel, *Environ. Sci. Pollut. Res.*, 2022, 22461, DOI: **10.1007/s11356-022-22461-7**.

47 M. A. Salam, M. Mokhtar, S. M. Albukhari, D. F. Baamer, L. Palmisano and M. R. Abukhadra, Insight into the role of the zeolitization process in enhancing the adsorption performance of kaolinite/diatomite geopolymer for effective retention of Sr (II) ions; batch and column studies, *J. Environ. Manage.*, 2021, **294**, 112984, DOI: **10.1016/j.jenvman.2021.112984**.

48 Z. Dong, J. Liu, D. Wen, M. Zhai and L. Zhao, Aminomethylpyridine isomers functionalized cellulose microspheres for TcO4-/ReO4- uptake: Structure-properties relationship and their application in different aquatic systems, *J. Hazard. Mater.*, 2022, **433**, 128728, DOI: **10.1016/j.jhazmat.2022.128728**.

49 B. Abbou, I. Lebkiri, H. Ouaddari, A. El Amri, F. E. Achibat, L. Kadiri, A. Ouass, A. Lebkiri and E. H. Rifi, Improved removal of methyl orange dye by adsorption using modified clay: Combined experimental study using surface response methodology, *Inorg. Chem. Commun.*, 2023, **155**, 111127, DOI: **10.1016/J.INOCHE.2023.111127**.

50 Q. Li, M. Yi, L. Shao, Y. Kou, Y. Wei and K. Wang, CTAB modified metakaolin-based geopolymer microspheres for the selective adsorption and recovery of TcO4−/ReO4−, *Sep. Purif. Technol.*, 2024, **350**, 127853, DOI: **10.1016/j.seppur.2024.127853**.

51 D. Mohan, K. P. Singh and V. K. Singh, Trivalent chromium removal from wastewater using low cost activated carbon derived from agricultural waste material and activated carbon fabric cloth, *J. Hazard. Mater.*, 2006, **135**, 280–295, DOI: **10.1016/J.JHAZMAT.2005.11.075**.

52 D. G. Duff, S. M. C. Ross and D. H. Vaughan, Adsorption from solution: An experiment to illustrate the Langmuir adsorption isotherm, *J. Chem. Educ.*, 1988, **65**, 815–816, DOI: **10.1021/ED065P815**.

53 G. M. V. K. Konaganti, R. Kota and S. Patil, Adsorption of anionic dyes on chitosan grafted poly (alkyl methacrylate)s, *Chem. Eng. J.*, 2010, **158**, 393–401.

54 S. Banerjee, M. C. Chattopadhyaya and Y. Chandra Sharma, 2015, Removal of an azo dye (Orange G) from aqueous solution using modified sawdust, Iwaponline.Com. (n.d.).

55 S. Banerjee, R. K. Gautam, A. Jaiswal, P. K. Gautam and M. C. Chattopadhyaya, Study on adsorption behavior of Acid Orange 10 onto modified wheat husk, *Desalin. Water Treat.*, 2016, **57**, 12302–12315, DOI: **10.1080/19443994.2015.1046151**.

56 M. Y. Nassar, T. Y. Mohamed, I. S. Ahmed, N. M. Mohamed and M. Khatab, Hydrothermally Synthesized Co3O4, α-Fe2O3, and CoFe2O4 Nanostructures: Efficient Nano-adsorbents for the Removal of Orange G Textile Dye from Aqueous Media, *J. Inorg. Organomet. Polym. Mater.*, 2017, **27**, 1526–1537, DOI: **10.1007/S10904-017-0613-X/METRICS**.

57 A. Malik, A. Khan and M. Humayun, Preparation and chemical modification of rice husk char for the removal of a toxic dye (Orange G) from aqueous medium, *Z. Phys. Chem.*, 2019, **233**, 375–392, DOI: **10.1515/ZPCH-2018-1190/MACHINEREADABLECITATION/RIS**.

58 J. H. Deng, X. R. Zhang, G. M. Zeng, J. L. Gong, Q. Y. Niu and J. Liang, Simultaneous removal of Cd(II) and ionic dyes from aqueous solution using magnetic graphene oxide nanocomposite as an adsorbent, *Chem. Eng. J.*, 2013, **226**, 189–200, DOI: **10.1016/J.CEJ.2013.04.045**.

59 I. D. Mall, V. C. Srivastava and N. K. Agarwal, Removal of Orange-G and Methyl Violet dyes by adsorption onto bagasse fly ash—kinetic study and equilibrium isotherm analyses, *Dyes Pigm.*, 2006, **69**, 210–223, DOI: **10.1016/J.DYEPIG.2005.03.013**.

60 V. V. Dev, B. Wilson, K. K. Nair, S. Antony and K. A. Krishnan, Response surface modeling of Orange-G adsorption onto surface tuned ragi husk, *Colloid Interface Sci. Commun.*, 2021, **41**, 100363, DOI: **10.1016/J.COLCOM.2021.100363**.

61 H. Budiman and O. Zuas, Adsorption Isotherm Studies on Acid Orange-10 Dye Removal using Cerium Dioxide Nanoparticles, *Indones. J. Chem.*, 2014, **14**, 226–232, DOI: **10.22146/IJC.21232**.

62 M. A. Salam, S. A. Kosa and A. A. Al-Beladi, Application of nanoclay for the adsorptive removal of Orange G dye from aqueous solution, *J. Mol. Liq.*, 2017, **241**, 469–477, DOI: **10.1016/J.MOLLIQ.2017.06.055**.

63 N. M. Mubarak, Y. T. Fo, H. S. Al-Salim, J. N. Sahu, E. C. Abdullah, S. Nizamuddin, N. S. Jayakumar and P. Ganesan, Removal of Methylene Blue and Orange-G from Waste Water Using Magnetic Biochar, *Int. J. Nanosci.*, 2015, **14**, 1550009, DOI: **10.1142/S0219581X1550009X**.

64 Z. Zaheer, W. AbuBaker Bawazir, S. M. Al-Bukhari and A. S. Basaleh, Adsorption, equilibrium isotherm, and thermodynamic studies to the removal of acid orange 7, *Mater. Chem. Phys.*, 2019, **232**, 109–120, DOI: **10.1016/j.matchemphys.2019.04.064**.